

The influence of localised randomness on regular grazing bifurcations with applications to impacting dynamics.

D.J.W. Simpson[†] and R. Kuske[‡]

[†]Institute of Fundamental Sciences
Massey University
Palmerston North
New Zealand

[‡]Department of Mathematics
University of British Columbia
Vancouver, BC
Canada

February 11, 2015

Abstract

This paper concerns stochastic perturbations of piecewise-smooth ODE systems relevant for vibro-impacting dynamics, where impact events constitute the primary source of randomness. Such systems are characterised by the existence of switching manifolds that divide the phase space into regions where the system is smooth. The initiation of impacts is captured by a grazing bifurcation, at which a periodic orbit describing motion without impacts develops a tangential intersection with a switching manifold. Oscillatory dynamics near regular grazing bifurcations are described by piecewise-smooth maps involving a square-root singularity, known as Nordmark maps. We consider three scenarios where coloured noise only affects impacting dynamics, and derive three two-dimensional stochastic Nordmark maps with the noise appearing in different nonlinear or multiplicative ways, depending on the source of the noise. Consequently the stochastic dynamics differs between the three noise sources, and is fundamentally different to that of a Nordmark map with additive noise. This critical dependence on the nature of the noise is illustrated with a prototypical one-degree-of-freedom impact oscillator.

1 Introduction

Many vibrating mechanical systems experience undesirable impacts that cause wear or sub-optimal performance. Occasional impacts may be permissible if they result from running components of the system at high speeds for greater efficiency, and some impacts are unavoidable

such as those due to random or rare events. In these cases it is important to have a clear understanding of the dynamical behaviour that impacts may induce. Impacting dynamics is often complicated or chaotic because impacts are highly nonlinear phenomena [1, 2, 3, 4, 5].

For instance tubes in heat exchangers vibrate at high fluid velocities and impact against baffles in place to guide the fluid flow. Simple mathematical models of heat exchangers reveal that chaotic dynamics may be created at the onset of recurring impacts [6, 7]. Rotating cutters spun at high speeds experience repeated contact loss with the material being cut. The resulting impacts between the cutter and the material may similarly induce chaotic dynamics [8, 9, 10]. In contrast, some mechanical systems use impacts to achieve their function. Atomic force microscopes measure surface topography and the chemical properties of a sample on the nanoscale by gently hitting the sample with a vibrating cantilever. In this context it is important to understand the complex impacting dynamics so that the inverse problem of describing the sample can be performed effectively [11, 12, 13].

Impacts can often be modelled accurately by carefully describing the deformations that components of the system undergo during impacts [14, 15]. However, for the purposes of understanding vibro-impacting dynamics, such a modelling approach is too cumbersome and a low degree-of-freedom ODE model can be more useful. Despite the low-dimensionality, such models have been shown to quantitatively match the experimental data of a variety of impacting systems. Examples include a cam-follower system involving occasional detachments between the cam and the follower [16, 17], a pendulum experiencing near-instantaneous impacts with a solid wall [18], and compliant impacts of a steel block with an elastic beam [19, 20, 21].

Using a low degree-of-freedom ODE model, the evolution of the system between impacts is tracked in phase space. Periodic behaviour without impacts corresponds to a periodic orbit in phase space that does not reach the switching manifold, Σ , Fig. 1-A. Physically, Σ corresponds to locations or instances where mechanical components come into contact, or lose contact. As parameters vary, the system may transition from an impact-free regime to the repeated (though not necessarily regular) occurrence of impacts. In phase space, the transition occurs when the periodic orbit of the ODE model attains an intersection with Σ , Fig. 1-B. This is known as a *grazing bifurcation*.

In this paper we study grazing bifurcations of the three-dimensional piecewise-smooth ODE

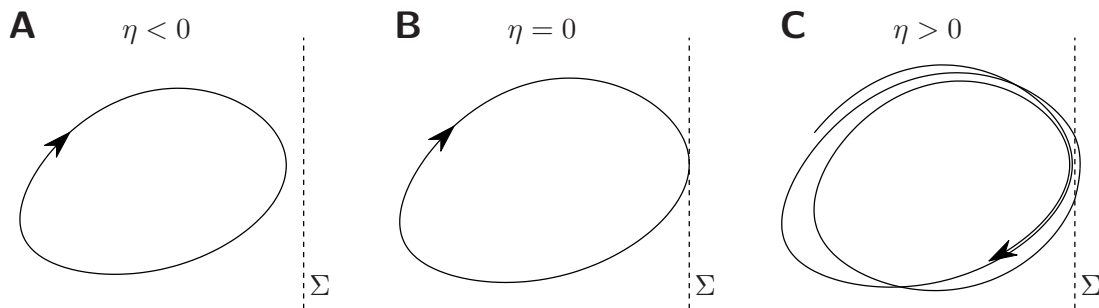


Figure 1: Sketches of phase space illustrating a regular grazing bifurcation occurring at $\eta = 0$, where $\eta \in \mathbb{R}$ is a system parameter.

system,

$$\begin{bmatrix} \dot{u} \\ \dot{v} \\ \dot{w} \end{bmatrix} = \begin{cases} f_L(u, v, w; \eta) , & u < 0 \\ f_R(u, v, w; \eta) , & u > 0 \end{cases} , \quad (1.1)$$

where f_L and f_R are smooth functions, $\eta \in \mathbb{R}$ is a parameter, and the coordinates (u, v, w) are chosen so that Σ is simply the coordinate plane $u = 0$. We assume that for $\eta < 0$, there exists an attracting periodic orbit describing non-impacting dynamics located entirely in the region $u < 0$, and that the periodic orbit grazes Σ at the origin when $\eta = 0$. In the context of vibro-impacting systems, $u < 0$ corresponds to not-in-contact dynamics governed by f_L , and $u > 0$ corresponds to in-contact dynamics governed by f_R . Impacts may instead be modelled as instantaneous events with energy loss and velocity reversal, in which case a map is usually defined on the switching manifold to describe the action of an impact [22].

Theoretical studies of piecewise-smooth and hybrid dynamical systems have led to a useful classification of grazing bifurcations [23]. This paper concerns regular grazing bifurcations. The grazing bifurcation of (1.1) at $\eta = 0$ is said to be *regular* if

$$\text{sgn} \left(e_1^\top f_L(0, v, w; \eta) \right) = \text{sgn} \left(e_1^\top f_R(0, v, w; \eta) \right) , \quad (1.2)$$

for all $(v, w; \eta)$ in a neighbourhood of $(0, 0; 0)$. This condition arises naturally in mechanical systems with compliant impacts, and implies that Σ is neither attracting nor repelling at any point.

As indicated in Fig. 1-C, the steady-state dynamics of (1.1) for $\eta > 0$ is often complicated. For this reason it is valuable to study the oscillatory dynamics using a return map based on the points on a Poincaré section. A normal form for such a map for regular grazing in \mathbb{R}^3 is the Nordmark map

$$\begin{bmatrix} x_{i+1} \\ y_{i+1} \end{bmatrix} = \begin{cases} g(x_i, y_i) , & x_i \leq 0 \\ g(x_i, y_i) - \begin{bmatrix} \chi \sqrt{x_i} \\ 0 \end{bmatrix} , & x_i \geq 0 \end{cases} , \quad (1.3)$$

where

$$g(x, y) = \begin{bmatrix} \tau & 1 \\ -\delta & 0 \end{bmatrix} \begin{bmatrix} x \\ y \end{bmatrix} + \begin{bmatrix} 0 \\ 1 \end{bmatrix} \mu , \quad (1.4)$$

with $\tau, \delta \in \mathbb{R}$, and $\chi = \pm 1$, as determined by the sign of certain coefficients, see §2. The coordinates (x, y) represent points on a Poincaré section of (1.1), with $\mu \in \mathbb{R}$ the bifurcation parameter and the grazing bifurcation occurring at $\mu = 0$. The Nordmark map (1.3), applicable also to models with instantaneous impacts [24, 25], includes only the leading order terms of the return map, so is valid only for dynamics close to the grazing bifurcation [23].

Each iteration of (1.3) corresponds to one oscillation of (1.1) near the grazing periodic orbit. The utility of (1.3) lies in the fact that the nature of the dynamics can be identified by the location of the corresponding points in the (μ, x) -plane. Specifically, (1.3) is formulated so that if $x_i < 0$ then the oscillation lies entirely in $u < 0$, and if $x_i > 0$ then the oscillation enters $u > 0$. The non-impacting, attracting periodic orbit shown in Fig. 1-A corresponds to the fixed point of g ,

$$\begin{bmatrix} x^L \\ y^L \end{bmatrix} = \frac{1}{\delta - \tau + 1} \begin{bmatrix} 1 \\ 1 - \tau \end{bmatrix} \mu , \quad (1.5)$$

with $x^L < 0$ and $\mu < 0$.

More generally, a periodic orbit of (1.1) appears as a finite set of points in the (μ, x) plane, as in Fig. 2 which shows a typical bifurcation diagram of (1.3). This figure shows a period-incrementing cascade, corresponding to several different periodic orbits, and apparently chaotic dynamics, as indicated by a cloud of points. For alternate values of τ and δ , the fixed point (x^L, y^L) may bifurcate directly to chaos [23, 26]. The square-root term in (1.3) is an artifact of the tangency between the periodic orbit and the switching manifold of (1.1) at the grazing bifurcation, and is responsible for the distinctive shape of the bifurcation diagram near $\mu = 0$. For some vibro-impacting systems it is more appropriate for the return map to be piecewise-linear and either continuous [27] or discontinuous [28]. Such maps predict fundamentally different bifurcation structures to those of (1.3).

In order to properly explain complicated vibro-impacting dynamics, the effects of randomness and uncertainties needs to be taken into account. Mechanical systems are subject to background vibrations and other sources of noise. Experimentally measured parameters involve error, and some physical features are left unmodelled. For instance, one-degree-of-freedom models do not capture high frequency modes that are often excited by impacts [29].

To quantitatively describe stochastic impacting dynamics, stochastic averaging methods have proved useful for vibro-impacting systems that experience a wide range of impact velocities [30, 31, 32, 33]. If only low-velocity impacts are relevant, then it is useful to study (1.3). In his PhD thesis [34], Griffin studied (1.3) in the presence of additive white noise. He found that noise blurs bifurcation diagrams and washes out high-period solutions in the same manner as for

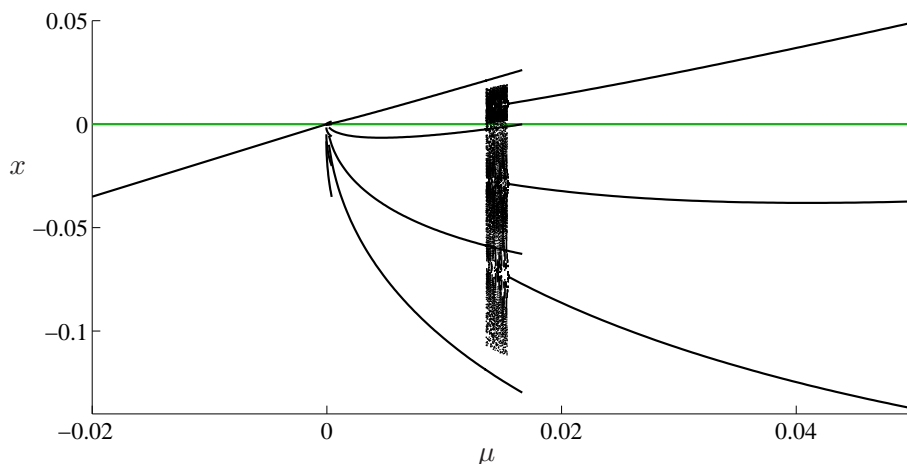


Figure 2: A bifurcation diagram of the Nordmark map (1.3) with $\tau \approx 0.5813$, $\delta \approx 0.1518$, and $\chi = 1$. These parameter values correspond to the vibro-impacting system described in §3, with $(k_{\text{osc}}, b_{\text{osc}}, k_{\text{supp}}, b_{\text{supp}}, d) = (4.5, 0.3, 10, 0, 0.1)$. The fixed point of (1.3) for $\mu < 0$, given by (1.5), corresponds to an attracting, non-impacting periodic orbit of period 2π . The map (1.3) has attracting 3 and 4-cycles for certain values of $\mu > 0$ as shown, as well as an attracting 5-cycle in the approximate range, $-0.00004 < \mu < 0.00041$. These correspond to periodic orbits of period approximately equal to $2k\pi$, for $k = 3, 4, 5$, that experience one impact per period. There also appears to be a chaotic attractor for the approximate range, $0.0135 < \mu < 0.0155$.

smooth maps, such as the logistic map [35, 36]. Recently it was shown that white noise added to (1.1) translates to additive white noise in (1.3), [37]. Such a noise formulation may be sensible for vibro-impacting systems for which a forcing term or external fluctuations represent a significant source of uncertainty.

However, impact events themselves constitute a substantial source of randomness. The purpose of this paper is to construct and analyse stochastic versions of (1.3) for which randomness stems purely from impact events. We consider three different types of impact noise for (1.1) using an Ornstein-Uhlenbeck process with stationary density $\mathcal{N}\left[0, \frac{\varepsilon^2}{2\nu}\right]$, where $\varepsilon \ll 1$ represents the noise amplitude and $\nu > 0$ is the correlation time. We first consider uncertainties in Σ , then uncertainties in f_R , and lastly uncertainties in f_R in the white noise (zero correlation time) limit.

Here let us indicate the forms of the stochastic maps that we obtain. Coloured noise in Σ leads to random perturbations in both the map and the switching condition as

$$\begin{bmatrix} x_{i+1} \\ y_{i+1} \end{bmatrix} = N_1(x_i, y_i) = \begin{cases} g(x_i, y_i) , & x_i + \kappa_1 \xi_i \leq 0 \\ g(x_i, y_i) - \begin{bmatrix} \chi \sqrt{x_i + \kappa_1 \xi_i} \\ 0 \end{bmatrix} , & x_i + \kappa_1 \xi_i \geq 0 \end{cases} , \quad (1.6)$$

where $\xi_i \in \mathbb{R}$ are Gaussian random variables, and $\kappa_1 > 0$ is a constant. For coloured noise in the impacting dynamics we obtain

$$\begin{bmatrix} x_{i+1} \\ y_{i+1} \end{bmatrix} = N_2(x_i, y_i) = \begin{cases} g(x_i, y_i) , & x_i \leq 0 \\ g(x_i, y_i) - \begin{bmatrix} \chi \kappa_2(\xi_i) \sqrt{x_i} \\ 0 \end{bmatrix} , & x_i \geq 0 \end{cases} , \quad (1.7)$$

for a particular nonlinear function κ_2 . For white noise ($\nu \rightarrow 0$) in the impacting dynamics the map takes the form

$$\begin{bmatrix} x_{i+1} \\ y_{i+1} \end{bmatrix} = N_3(x_i, y_i) = \begin{cases} g(x_i, y_i) , & x_i \leq 0 \\ g(x_i, y_i) - \begin{bmatrix} \chi \kappa_3(r_i, h_i) \sqrt{x_i} \\ 0 \end{bmatrix} + \kappa_4(h_i) x_i , & x_i \geq 0 \end{cases} , \quad (1.8)$$

where r_i and h_i are random variables, and $\kappa_3 : \mathbb{R}^2 \rightarrow \mathbb{R}$ and $\kappa_4 : \mathbb{R} \rightarrow \mathbb{R}^2$ are nonlinear functions. Notice that N_1 is stochastic for $x_i < 0$, whereas N_2 and N_3 are not. This is because noise in Σ generates anomalous crossings of $x_i = 0$. Consequently N_1 exhibits stochastic dynamics for $\mu < 0$, while N_2 and N_3 do not. N_2 and N_3 involve noise terms proportional to $\sqrt{x_i}$, and for this reason exhibit increasing variability for larger values of $\mu > 0$.

To obtain a more detailed comparison of N_1 , N_2 and N_3 , we first carefully derive (1.3) in §2. In §3 we introduce a prototypical compliant vibro-impacting system to illustrate our results. In §4 we add randomness and derive (1.6)-(1.8). Since (1.6)-(1.8) involve fundamentally different noise terms, they exhibit different sensitivities to the noise amplitude ε . Therefore we use different values of ε in each of the different models, in order to make appropriate comparisons. For each N_j ($j = 1, 2, 3$) we write $\varepsilon = \tilde{\varepsilon}_j \alpha$ and identify the appropriate value $\tilde{\varepsilon}_j$, so that N_1 , N_2 and N_3 display roughly the same dynamics for the vibro-impacting system with the parameters of Fig. 2 and $\mu = 0.03$ (chosen for illustration) and $\alpha = 1$. This enables us to quantitatively compare N_1 , N_2 and N_3 in §5. Conclusions are presented in §6.

2 A derivation of the Nordmark map

In this section we derive a return map for the generic deterministic system (1.1) valid near the grazing bifurcation $\eta = 0$ and provide an explicit coordinate change that transforms the map to (1.3). Such a derivation is given in [23, 38]. We provide an explicit construction of (1.3) here in order to provide a basis for deriving the stochastic maps in §4. Throughout this section we write $z = (u, v, w)$ for points of (1.1) in \mathbb{R}^3 .

As discussed in §1, we assume that with $\eta = 0$ the system (1.1) has a periodic orbit that intersects the origin, but is otherwise contained in $u < 0$. This implies that $\dot{u} = 0$ for f_L at the origin with $\eta = 0$ (i.e. $e_1^\top f_L(0, 0, 0; 0) = 0$). For simplicity, we assume that we further have

$$e_1^\top f_L(u, 0, w; \eta) = 0, \quad (2.1)$$

for all $(u, w; \eta)$ in a neighbourhood of $(0, 0; 0)$, which can usually be imposed by an appropriate coordinate change. This assumption is particularly useful in the case that randomness is present in the switching condition, see §4.1.

The key to deriving the Nordmark map (1.3) is selecting a convenient Poincaré section and constructing a *discontinuity map* that accounts for the difference between f_L and f_R , that is, the difference between impacting and non-impacting dynamics. We let Π represent a generic Poincaré section of (1.1) that lies in $u < 0$ and intersects the grazing periodic orbit transversally, and let Π' be the coordinate plane $v = 0$, see Fig. 3.

Given $z_0 \in \Pi$, we define $z_1 \in \Pi'$ as the next intersection of the forward orbit governed by f_L (i.e. ignoring the switching condition at $u = 0$) with Π' . If $u > 0$ for the point z_1 , then z_1 does not represent the true intersection of the orbit of (1.1) with Π . Nevertheless, we study the

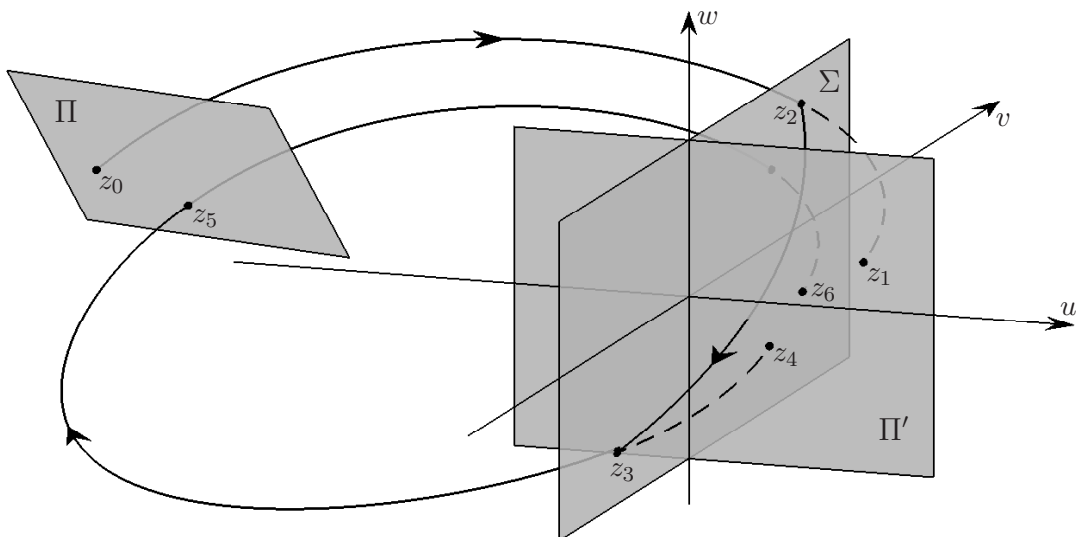


Figure 3: A schematic diagram illustrating the construction of the Nordmark map (1.3) for the three-dimensional piecewise-smooth system (1.1). The solid curve represents an orbit of (1.1). The dashed curves show virtual extensions of this orbit into $u > 0$ as governed by f_L .

return map on Π' ($z_1 \rightarrow z_6$) rather than the return map on Π ($z_0 \rightarrow z_5$), because the two maps are conjugate and the map on Π' has a simpler form than the map on Π .

To derive the return map on Π' , we must consider three additional points, z_2 , z_3 , and z_4 , see Fig. 3. The points z_2 and z_3 correspond to the entry and exit locations of the orbit with the impacting region, $u > 0$. Then z_1 is obtained by travelling forward from the entry point z_2 to Π' using f_L , whilst z_4 is obtained by travelling backward from the exit point z_3 to Π' using f_L . The discontinuity map is defined as $z_4 = D(z_1)$. If $u \leq 0$ for the point z_1 , then $z_4 = z_1$.

In order to derive an explicit expression for the discontinuity map, we consider the three steps, $z_1 \rightarrow z_2$, $z_2 \rightarrow z_3$, and $z_3 \rightarrow z_4$, individually, and expand f_L and f_R about $\eta = 0$ and the origin by writing

$$f_J(u, v, w; \eta) = \begin{bmatrix} \alpha_J v + \mathcal{O}(2) \\ -\beta_J + \mathcal{O}(1) \\ \gamma_J + \mathcal{O}(1) \end{bmatrix}, \quad (2.2)$$

where $\alpha_J, \beta_J, \gamma_J \in \mathbb{R}$, and $J = L, R$. In (2.2), and throughout this section, $\mathcal{O}(k)$ is short-hand big-O notation for $\mathcal{O}((\sqrt{u}, v, w, \eta)^k)$. Notice that \sqrt{u} is assumed to be of the same order as v , w , and η , which is appropriate in view of the tangency between the grazing periodic orbit and Σ . We assume

$$\alpha_L, \alpha_R, \beta_L, \beta_R > 0, \quad (2.3)$$

such that the tangency is quadratic for both f_L and f_R , and has the orientation depicted in Fig. 3.

From series expansions of the orbits governed by f_L and f_R , see [23, 38], we obtain the following formulas for the three steps in the discontinuity map in the case $u_1 > 0$ (writing $z_i = (u_i, v_i, w_i)$). For $z_1 \rightarrow z_2$,

$$\begin{bmatrix} v_2 \\ w_2 \end{bmatrix} = \begin{bmatrix} \frac{\sqrt{2\beta_L}}{\sqrt{\alpha_L}} \sqrt{u_1} + \mathcal{O}(2) \\ w_1 - \frac{\sqrt{2\gamma_L}}{\sqrt{\alpha_L \beta_L}} \sqrt{u_1} + \mathcal{O}(2) \end{bmatrix}, \quad (2.4)$$

for $z_2 \rightarrow z_3$,

$$\begin{bmatrix} v_3 \\ w_3 \end{bmatrix} = \begin{bmatrix} -v_2 + \mathcal{O}(2) \\ w_2 + \frac{2\gamma_R}{\beta_R} v_2 + \mathcal{O}(2) \end{bmatrix}, \quad (2.5)$$

and for $z_3 \rightarrow z_4$,

$$\begin{bmatrix} u_4 \\ w_4 \end{bmatrix} = \begin{bmatrix} \frac{\alpha_L}{2\beta_L} v_3^2 + \mathcal{O}(3) \\ w_3 + \frac{\gamma_L}{\beta_L} v_3 + \mathcal{O}(2) \end{bmatrix}. \quad (2.6)$$

By combining (2.4)-(2.6) we get (u_4, w_4) in terms of (u_1, w_1) ,

$$\begin{bmatrix} u_4 \\ w_4 \end{bmatrix} = \begin{bmatrix} u_1 + \mathcal{O}(3) \\ w_1 - c\sqrt{u_1} + \mathcal{O}(2) \end{bmatrix}, \quad (2.7)$$

where

$$c = \frac{2\sqrt{2\beta_L}}{\sqrt{\alpha_L}} \left(\frac{\gamma_L}{\beta_L} - \frac{\gamma_R}{\beta_R} \right). \quad (2.8)$$

The discontinuity map is then

$$D(u, w; \eta) = \begin{cases} \begin{bmatrix} u \\ w \end{bmatrix}, & u \leq 0 \\ \begin{bmatrix} u + \mathcal{O}(3) \\ w - c\sqrt{u} + \mathcal{O}(2) \end{bmatrix}, & u \geq 0 \end{cases}. \quad (2.9)$$

To complete the map (1.3), which represents $z_1 \rightarrow z_6$ as shown in Fig. 3, we must combine $D(z_1)$ with the global return map $z_6 = G(z_4)$. G depends on global properties of f_L and is smooth, so we can write

$$G(u, w; \eta) = A \begin{bmatrix} u \\ w \end{bmatrix} + b\eta + \mathcal{O}((u, w, \eta)^2), \quad (2.10)$$

for some

$$A = \begin{bmatrix} a_{11} & a_{12} \\ a_{21} & a_{22} \end{bmatrix}, \quad b = \begin{bmatrix} b_1 \\ b_2 \end{bmatrix}, \quad (2.11)$$

where each $a_{ij}, b_i \in \mathbb{R}$. Then the desired return map on Π' is the composition $G \circ D$.

Finally we apply a coordinate change to convert the map to the normal form (1.3) that involves only three parameters, τ , δ and χ . Under

$$\begin{bmatrix} x \\ y \\ \mu \end{bmatrix} = \frac{1}{a_{12}^2 c^2} \begin{bmatrix} 1 & 0 & 0 \\ -a_{22} & a_{12} & b_1 \\ 0 & 0 & (1 - a_{22})b_1 + a_{12}b_2 \end{bmatrix} \begin{bmatrix} u \\ w \\ \eta \end{bmatrix}, \quad (2.12)$$

and with higher order terms omitted, $G \circ D$ transforms to (1.3) with

$$\tau = \text{trace}(A), \quad \delta = \det(A), \quad \chi = \text{sgn}(a_{12}c). \quad (2.13)$$

Since the Nordmark map keeps only leading order terms for $(u, w; \eta)$ near $(0, 0; 0)$, terms that are linear in x are omitted since they are dominated by \sqrt{x} , refer to [39] for a further discussion. In (2.12) we require $a_{12} \neq 0$ and $c \neq 0$. These represent non-degeneracy conditions for the grazing bifurcation.

3 An oscillator with compliant impacts

To motivate and illustrate our results for stochastic Nordmark maps, we consider the prototypical vibro-impacting system shown in Fig. 4 and studied in [37, 40, 41]. This system consists of a harmonically forced one-degree-of-freedom linear oscillator that experiences compliant (or soft) impacts with a support, and we use the following non-dimensionalised equations to model the dynamics:

$$\ddot{u} = \begin{cases} -k_{\text{osc}}(u + 1) - b_{\text{osc}}\dot{u} + F \cos(t), & u < 0 \\ -k_{\text{osc}}(u + 1) - (b_{\text{osc}} + b_{\text{supp}})\dot{u} - k_{\text{supp}}(u + d) + F \cos(t), & u > 0 \end{cases}. \quad (3.1)$$

Here $u(t)$ denotes the location of the block, which has the equilibrium position $u = -1$. A rigid stop prevents the support reaching a position with $u < 0$, and prestresses the support by a distance, $d > 0$. The constants k_{osc} , b_{osc} , k_{supp} and b_{supp} represent non-dimensionalised spring and damping coefficients for the oscillator and support. We neglect the mass of the support, ignore energy loss at impacts, and assume that whenever the block is not in contact with the support, the support is located at $u = 0$. Experiments of simple vibro-impacting systems with compliant impacts have shown that low-dimensional models such as (3.1) can quantitatively match the physically observed dynamics near grazing bifurcations [19, 20, 21].

Here we treat the forcing amplitude, $F > 0$, as the primary bifurcation parameter, and assume $k_{\text{osc}}, b_{\text{osc}} > 0$. The steady-state solution (behaviour in the limit $t \rightarrow \infty$) to (3.1) with $u < 0$ is

$$u_{\text{ss}}(t) = -1 + \frac{(k_{\text{osc}} - 1) \cos(t) + b_{\text{osc}} \sin(t)}{(k_{\text{osc}} - 1)^2 + b_{\text{osc}}^2} F. \quad (3.2)$$

When $F < F_{\text{graz}}$, where

$$F_{\text{graz}} = \sqrt{(k_{\text{osc}} - 1)^2 + b_{\text{osc}}^2}, \quad (3.3)$$

the maximum value of $u_{\text{ss}}(t)$ over one period is negative, and so $u_{\text{ss}}(t)$ is an attracting non-impacting periodic orbit of (3.1). The critical value, $F = F_{\text{graz}}$, is a grazing bifurcation at which $u_{\text{ss}}(t)$ has unit amplitude and attains the value $u = 0$ at times $t = t_{\text{graz}} + 2\pi k$, for $k \in \mathbb{Z}$, where

$$t_{\text{graz}} = \tan^{-1} \left(\frac{b_{\text{osc}}}{k_{\text{osc}} - 1} \right), \quad (3.4)$$

and $0 < t_{\text{graz}} < \pi$.

To convert (3.1) to the general form (1.1), we define

$$v = \dot{u}, \quad w = (t \bmod 2\pi) - t_{\text{graz}}, \quad \eta = F - F_{\text{graz}}. \quad (3.5)$$

Here the phase space of (3.1) with (3.5) is isomorphic to $\mathbb{R}^2 \times \mathbb{T}$, rather than \mathbb{R}^3 , but this does not affect the bifurcation structure near grazing. For (3.1) with (3.5), the coefficients in (2.2),

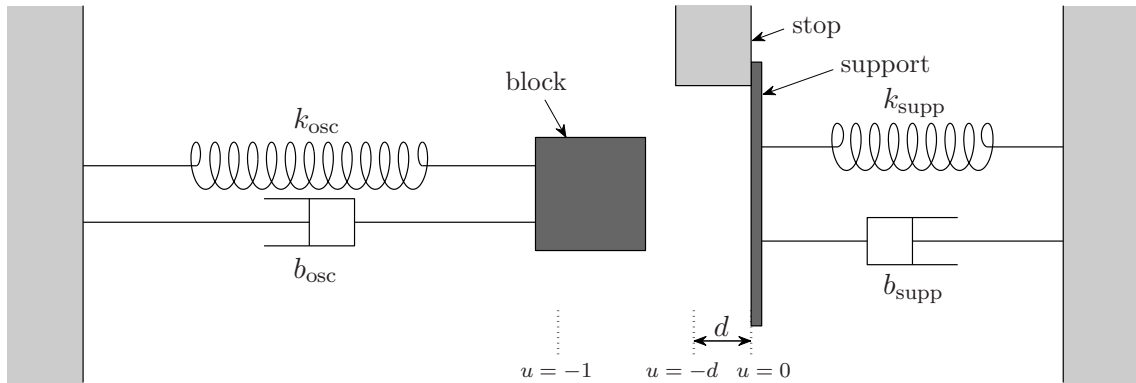


Figure 4: A schematic diagram of the vibro-impacting system modelled by (3.1). This system exhibits a *regular* grazing bifurcation with a square-root singularity because with $k_{\text{supp}} > 0$ and $d > 0$ the equations of motion are discontinuous at the grazing point.

which describe the behaviour of the system near the grazing point, are given by

$$\begin{aligned} \alpha_L &= 1, & \beta_L &= 1, & \gamma_L &= 1, \\ \alpha_R &= 1, & \beta_R &= 1 + k_{\text{supp}}d, & \gamma_R &= 1, \end{aligned} \quad (3.6)$$

and by evaluating (2.8) with (3.6) we obtain

$$c = \frac{2\sqrt{2}k_{\text{supp}}d}{1 + k_{\text{supp}}d}. \quad (3.7)$$

In addition, from the general solution to (3.1) we find that the coefficients in the global map (2.10) are given by

$$A = \exp\left(2\pi \begin{bmatrix} 0 & 1 \\ -k_{\text{osc}} & -b_{\text{osc}} \end{bmatrix}\right), \quad b = \frac{1}{F_{\text{graz}}} \begin{bmatrix} 1 - a_{11} \\ -a_{21} \end{bmatrix}. \quad (3.8)$$

4 Incorporating randomness into the Nordmark map

To model noise and uncertainties we use the one-dimensional Ornstein-Uhlenbeck process

$$d\xi(t) = -\frac{1}{\nu}\xi(t)dt + \frac{\varepsilon}{\nu}dW(t), \quad (4.1)$$

where $\varepsilon, \nu > 0$ are constants and $W(t)$ is a standard Brownian motion. Given an initial value $\xi(0) = \xi_0$, at any positive time $\xi(t)$ is a Gaussian random variable with mean and variance

$$\mathbb{E}[\xi(t)|\xi(0) = \xi_0] = \xi_0 e^{-\frac{t}{\nu}}, \quad \text{Var}[\xi(t)|\xi(0) = \xi_0] = \frac{\varepsilon^2}{2\nu} \left(1 - e^{-\frac{2t}{\nu}}\right). \quad (4.2)$$

In the limit $t \rightarrow \infty$, $\xi(t) \sim \mathcal{N}\left[0, \frac{\varepsilon^2}{2\nu}\right]$, where $\mathcal{N}[\mu, \sigma^2]$ denotes the Gaussian distribution of mean μ and variance σ^2 . The *correlation time* of (4.1), defined as $\int_0^\infty \frac{\mathbb{E}[\xi(t)\xi(0)]}{\text{Var}[\xi(0)]} dt$, with $\xi(0) \sim \mathcal{N}\left[0, \frac{\varepsilon^2}{2\nu}\right]$, is equal to ν .

In our context, $\xi(t)$ is coloured noise and the parameter ε governs the size of the noise. Unlike white noise, $\xi(t)$ has an inherent time-scale, ν , and is suitable for modelling various types of uncertainties in mechanical systems, such as background vibrations [42]. In the white noise limit, forcing by $\xi(t)$ becomes a diffusion process $\varepsilon dW(t)$.

4.1 Stochastic switching

We first consider the following stochastic perturbation of (1.1),

$$\begin{bmatrix} \dot{u} \\ \dot{v} \\ \dot{w} \end{bmatrix} = \begin{cases} f_L(u, v, w; \eta), & u + \xi(t) < 0 \\ f_R(u, v, w; \eta), & u + \xi(t) > 0 \end{cases}, \quad (4.3)$$

where $\xi(t)$ is given by (4.1). In (4.3) randomness is present in the switching condition, while evolution between switching events remains deterministic. We expect (4.3) to be applicable to a wide variety of piecewise-smooth systems. For the vibro-impacting system of §3, $\xi(t)$ may capture uncertainties in the point at which contact between the block and support occurs or is lost. For switched control systems, $\xi(t)$ may correspond to measurement errors that produce variability in evaluations of switching rules [43, 44].

Here we consider orbits of (4.3) that are close to the grazing periodic orbit of (1.1). Orbits of (4.3) near grazing only spend short lengths of time in the region $u > 0$ while passing near the origin, and for simplicity we suppose that the value of ν is large compared to such times. In this case it is reasonable to approximate $\xi(t)$ by a constant while an orbit is near the origin. With this approximation, the sum $u(t) + \xi(t)$ does not switch sign more than twice as the orbit passes near the origin, which substantially simplifies our calculations below.

We let ξ_i denote the value of $\xi(t)$ during the i^{th} instance that the orbit of (4.3) passes near the origin. The time between consecutive traversals near the origin is well-approximated by the period of the grazing periodic orbit, call it T . With this approximation,

$$\xi_i \sim \mathcal{N} \left[\xi_{i-1} e^{-\frac{T}{\nu}}, \frac{\varepsilon^2}{2\nu} \left(1 - e^{-\frac{2T}{\nu}} \right) \right]. \quad (4.4)$$

To derive the stochastic version of (1.3) for (4.3) with (4.4), we first derive the induced stochastic discontinuity map. Here condition (2.1) is useful, as it implies that an orbit governed by f_L attains a local maximum value of u at an intersection with Π' . For $u_1 + \xi_i \leq 0$, we conclude that $u(t) + \xi_i \leq 0$ as the orbit passes near the origin, so that $u_4 = u_1$. If instead $u_1 + \xi_i > 0$, then the discontinuity map D is given by (2.7) except that $u + \xi_i$ appears inside the square root because this quantity represents the distance from the switching condition. That is,

$$\begin{bmatrix} u_4 \\ w_4 \end{bmatrix} = \begin{bmatrix} u_1 + \mathcal{O}(3) \\ w_1 - c\sqrt{u_1 + \xi_i} + \mathcal{O}(2) \end{bmatrix}, \quad (4.5)$$

where $\mathcal{O}(k) = \mathcal{O} \left(\left(\sqrt{u}, \sqrt{|\xi_i|}, v, w, \eta \right)^k \right)$. By combining (4.5) with the global map G , applying the coordinate change (2.12), and dropping higher order terms, we obtain

$$\begin{bmatrix} x_{i+1} \\ y_{i+1} \end{bmatrix} = N_1(x_i, y_i) = \begin{cases} \begin{bmatrix} \tau & 1 \\ -\delta & 0 \end{bmatrix} \begin{bmatrix} x_i \\ y_i \end{bmatrix} + \begin{bmatrix} 0 \\ 1 \end{bmatrix} \mu, & x_i + \frac{\xi_i}{a_{12}^2 c^2} \leq 0 \\ \begin{bmatrix} \tau & 1 \\ -\delta & 0 \end{bmatrix} \begin{bmatrix} x_i \\ y_i - \chi \sqrt{x_i + \frac{\xi_i}{a_{12}^2 c^2}} \end{bmatrix} + \begin{bmatrix} 0 \\ 1 \end{bmatrix} \mu, & x_i + \frac{\xi_i}{a_{12}^2 c^2} \geq 0 \end{cases}. \quad (4.6)$$

N_1 is the stochastic Nordmark map corresponding to (4.3). Notice that randomness in the switching condition of (4.3) has translated to randomness in both the switching condition of (1.3) and in the image of the map with $x_i > 0$. In contrast, a piecewise-linear map for which randomness is present purely in the switching condition is studied in [45].

In order to fairly compare N_1 with other stochastic versions of (1.3) in §5, we estimate the effective size of the stochastic contribution for our illustrative parameters values of the prototypical system (3.1) and a representative value of $\mu = 0.03$. This motivates us to express ε in terms

of a scaled parameter $\varepsilon = \tilde{\varepsilon}_1 \alpha$, and to obtain comparable stochastic contributions for fixed α in the different cases. The square-root term of N_1 is $\sqrt{x_i + \kappa_1 \xi_i}$, where $\kappa_1 = \frac{1}{a_{12}^2 c^2}$. If x_i is large relative to $\kappa_1 \xi_i$, then this term is well-approximated by $\sqrt{x_i} + \frac{\xi_i}{2a_{12}^2 c^2 \sqrt{x_i}}$, and so $\frac{\xi_i}{2a_{12}^2 c^2 \sqrt{x_i}}$ estimates the additive stochastic contribution to N_1 . For the impact oscillator with the parameter values of Fig. 2 (here $c = \sqrt{2}$ and $a_{12} \approx 0.1227$) and using $x_i = 0.025$ (corresponding to the value of $x_i > 0$ in Fig. 2 for $\mu = 0.03$), this quantity is approximately $100\xi_i$. With $\nu = 0.5$ (used in §5), the standard deviation of the stochastic contribution is approximately 100ε . Therefore, for $\varepsilon = \tilde{\varepsilon}_1 \alpha$, where

$$\tilde{\varepsilon}_1 = 0.0001, \quad (4.7)$$

the standard deviation of the stochastic contribution is approximately 0.01 when $\alpha = 1$.

To illustrate the accuracy of N_1 , Fig. 5 compares iterates of N_1 (black dots) with a numerical solution to (4.3) for the vibro-impacting system of §3 (purple dots) using $\varepsilon = \tilde{\varepsilon}_1$. For the given parameter values, the system has an attracting 3-cycle in the absence of noise. For this reason, both sets of points are grouped about the 3-cycle. The two sets of points are slightly separated. This is because the form of the deterministic Nordmark map does not include higher order terms of the true return map, as observed by the separation of the values taken by the deterministic 3-cycles shown in Fig. 5. The size and shape of the spread of the two sets of randomly generated points are similar, as is their location relative to the deterministic values of the map. This demonstrates that N_1 can accurately capture the stochastic dynamics of (4.3). A more precise characterisation of the accuracy of N_1 is beyond the scope of this paper.

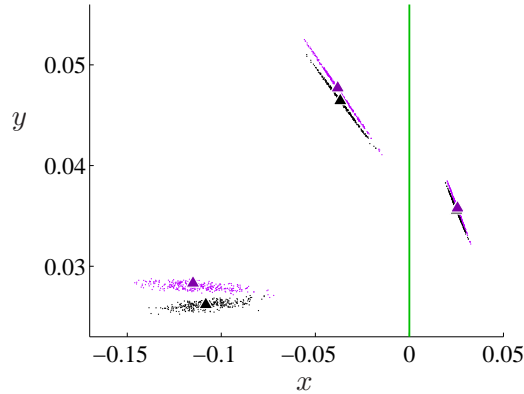


Figure 5: A phase portrait comparing the stochastic return map N_1 , (4.6), with a numerical solution to (4.3). The three groups of purple dots were obtained by numerically solving (4.3) with (4.1), $\nu = 0.5$ and $\varepsilon = \tilde{\varepsilon}_1$, for the vibro-impacting system (3.1) with (3.5) and $(k_{\text{osc}}, b_{\text{osc}}, k_{\text{supp}}, b_{\text{supp}}, d) = (4.5, 0.3, 10, 0, 0.1)$ (as in Fig. 2) and $F \approx F_{\text{graz}} + 0.005558$ (which corresponds to $\mu = 0.03$). More precisely, 1000 points on Π' (labelled z_1 in Fig. 3) were obtained by numerically solving (4.3), and these were transformed to (x, y) -coordinates by applying (2.12) and (3.5) to produce the purple dots. The three groups of black dots are 1000 iterates of N_1 with (4.4) and parameter values chosen to match the vibro-impacting system (specifically, $\nu = 0.5$, $\varepsilon = \tilde{\varepsilon}_1$, $T = 2\pi$, $\mu = 0.03$, $\tau \approx 0.5813$, $\delta \approx 0.1518$, $\chi = 1$, $c = \sqrt{2}$ and $a_{12} \approx 0.1227$). The deterministic 3-cycles of (4.3) and (4.6) are shown with triangles.

4.2 Additive coloured noise with a large correlation time

Next we consider the case where randomness and uncertainty in (1.1) is associated with f_R . For mechanical systems with impacts, this corresponds to variability in the evolution of the system during an impact. For simplicity we include noise in only the v -component of f_R , that is

$$\begin{bmatrix} \dot{u} \\ \dot{v} \\ \dot{w} \end{bmatrix} = \begin{cases} f_L(u, v, w; \eta), & u < 0 \\ f_R(u, v, w; \eta) + \begin{bmatrix} 0 \\ \xi(t) \\ 0 \end{bmatrix}, & u > 0 \end{cases}, \quad (4.8)$$

where $\xi(t)$ is given by (4.1). Indeed, for the vibro-impacting system of Fig. 4, if noise is incorporated into the force on the block when it is in contact with the support, then the equations of motion may be put in the form (4.8). With noise added to the u -component of f_R (or f_L), orbits may cross $u = 0$ many times in a short time frame which makes the system substantially more difficult to analyse. We leave such considerations for future work.

As in §4.1, we consider near-grazing orbits and assume that the value of ν is much larger than the time each orbit spends in the region $u > 0$. In this case it is reasonable to treat $\xi(t)$ as constant while $u > 0$. During the i^{th} instance that an orbit passes near the origin, we approximate $\xi(t)$ by ξ_i , distributed according to (4.4). In this scenario the three components of the discontinuity map (2.4)-(2.6) are unchanged except that β_R is replaced by $\beta_R - \xi_i$ in (2.5) (because the v -component of the system with $u > 0$ is given by $-\beta_R + \xi_i + \mathcal{O}(1)$, see (2.2)). By combining (2.4)-(2.6) we find that for $u_1 > 0$ the discontinuity map is given by

$$\begin{bmatrix} u_4 \\ w_4 \end{bmatrix} = \begin{bmatrix} u_1 + \mathcal{O}(3) \\ w_1 - c \left(\frac{\frac{\gamma_L}{\beta_L} - \frac{\gamma_R}{\beta_R - \xi_i}}{\frac{\gamma_L}{\beta_L} - \frac{\gamma_R}{\beta_R}} \right) \sqrt{u_1} + \mathcal{O}(2) \end{bmatrix}, \quad (4.9)$$

and therefore the corresponding stochastic Nordmark map is

$$\begin{bmatrix} x_{i+1} \\ y_{i+1} \end{bmatrix} = N_2(x_i, y_i) = \begin{cases} \begin{bmatrix} \tau & 1 \\ -\delta & 0 \end{bmatrix} \begin{bmatrix} x_i \\ y_i \end{bmatrix} + \begin{bmatrix} 0 \\ 1 \end{bmatrix} \mu, & x_i \leq 0 \\ \begin{bmatrix} \tau & 1 \\ -\delta & 0 \end{bmatrix} \begin{bmatrix} x_i \\ y_i - \chi \left(\frac{\frac{\gamma_L}{\beta_L} - \frac{\gamma_R}{\beta_R - \xi_i}}{\frac{\gamma_L}{\beta_L} - \frac{\gamma_R}{\beta_R}} \right) \sqrt{x_i} \end{bmatrix} + \begin{bmatrix} 0 \\ 1 \end{bmatrix} \mu, & x_i \geq 0 \end{cases}. \quad (4.10)$$

Notice that with $\xi_i = 0$, N_2 is identical to (1.3).

We can write the stochastic component of N_2 as $\chi \kappa_2(\xi_i) \sqrt{x_i}$, where $\kappa_2(\xi_i) = \frac{\frac{\gamma_L}{\beta_L} - \frac{\gamma_R}{\beta_R - \xi_i}}{\frac{\gamma_L}{\beta_L} - \frac{\gamma_R}{\beta_R}}$. With the parameter values of the impact oscillator (3.6), and $k_{\text{supp}} d = 1$, we have $\kappa_2(\xi_i) = 2 - \frac{2}{2 - \xi_i} \approx 1 - \frac{\xi_i}{2}$. Therefore the noise provides a multiplicative stochastic contribution of approximately $\frac{\sqrt{x_i} \xi_i}{2}$, ignoring signs. In order to compare the effect of the noise to the other cases, we write $\varepsilon = \tilde{\varepsilon}_2 \alpha$, choosing $\tilde{\varepsilon}_2$ so that the standard deviation of the stochastic contribution is 0.01 when $\alpha = 1$. For $x_i = 0.025$ and $\nu = 0.5$ (as in §4.1), the standard deviation of $\frac{\sqrt{x_i} \xi_i}{2}$ is approximately 0.08ε , so we therefore choose

$$\tilde{\varepsilon}_2 = 0.125. \quad (4.11)$$

Fig. 6 compares iterates of N_2 to intersections with Π' of a numerical solution to (4.8) using $\varepsilon = \tilde{\varepsilon}_2$. As expected the two sets of points are similarly distributed about the deterministic 3-cycle.

4.3 Additive coloured noise with a small correlation time

Lastly we consider (4.8) in the white noise limit, $\nu = 0$. In this case (4.8) reduces to a diffusion process forced by white noise, specifically $\xi(t) dt$ is replaced by $\varepsilon dW(t)$. By using (2.2) to expand f_R , (4.8) for $u > 0$ may be written as the three-dimensional stochastic differential equation

$$\begin{bmatrix} du(t) \\ dv(t) \\ dw(t) \end{bmatrix} = \begin{bmatrix} \alpha_R v(t) + \mathcal{O}(2) \\ -\beta_R + \mathcal{O}(1) \\ \gamma_R + \mathcal{O}(1) \end{bmatrix} dt + \varepsilon \begin{bmatrix} 0 \\ 1 \\ 0 \end{bmatrix} dW(t) . \quad (4.12)$$

To obtain a stochastic Nordmark map corresponding to this scenario, we first derive the stochastic version of the middle component of the discontinuity map (2.5). Given an initial point $(u(0), v(0), w(0)) = (0, v_2, w_2)$, where $v_2 > 0$ and $w_2 \in \mathbb{R}$ are small, the desired values of v_3 and w_3 are given by the point $(0, v_3, w_3)$ of *first return* for the stochastic process (4.12) to $u = 0$. First return or first passage problems are an important class of theoretical problems in stochastic calculus with applications traditionally in finance and chemical kinetics [46, 47, 48].

We approximate (4.12) by keeping only the leading order contributions, i.e.

$$\begin{bmatrix} du(t) \\ dv(t) \end{bmatrix} = \begin{bmatrix} \alpha_R v(t) \\ -\beta_R \end{bmatrix} dt + \varepsilon \begin{bmatrix} 0 \\ 1 \end{bmatrix} dW(t) , \quad \begin{bmatrix} u(0) \\ v(0) \end{bmatrix} = \begin{bmatrix} 0 \\ v_2 \end{bmatrix} , \quad (4.13)$$

together with $w(t) = w_2 + \gamma_R t$. With this approximation we are able to provide an explicit expression for the joint probability density function of the return location and time. A formal justification for the omission of the higher order terms is left for future work.

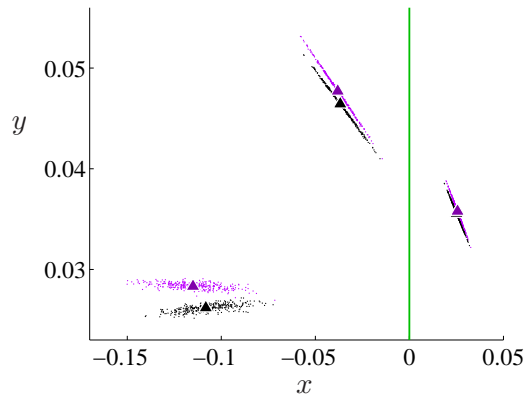


Figure 6: A phase portrait comparing the stochastic return map N_2 with a numerical solution to (4.8). The three groups of purple dots were obtained by numerically solving (4.8) with (4.1), $\nu = 0.5$ and $\varepsilon = \tilde{\varepsilon}_2$, for the vibro-impacting system (3.1) with (3.5) using the same parameter values as in Fig. 5. The three groups of black dots are 1000 iterates of N_2 with (4.4) and parameter values matching those of the vibro-impacting system (refer to the caption of Fig. 5). The deterministic 3-cycles of (4.3) and (4.6) are shown with triangles.

We introduce the change of variables

$$p = \frac{\beta_R}{\alpha_R v_2^2} u, \quad q = \frac{1}{v_2} v, \quad s = \frac{\beta_R}{v_2} t. \quad (4.14)$$

This puts (4.13) in a standard form studied in [49],

$$\begin{bmatrix} dp(s) \\ dq(s) \end{bmatrix} = \begin{bmatrix} q(s) \\ -1 \end{bmatrix} ds + \sqrt{\varrho} \begin{bmatrix} 0 \\ 1 \end{bmatrix} dW(s), \quad \begin{bmatrix} p(0) \\ q(0) \end{bmatrix} = \begin{bmatrix} 0 \\ 1 \end{bmatrix}, \quad (4.15)$$

where

$$\varrho = \frac{\varepsilon^2}{\beta_R v_2}. \quad (4.16)$$

Specifically, q is a diffusion process with constant drift, and $p(s) = \int_0^s q(\tilde{s}) d\tilde{s}$. Therefore $p(s)$ may be interpreted as *integrated Brownian motion with constant drift*.

We let $\mathcal{F}(r, h; \varrho)$ denote the joint probability density function for the first return of (4.15) to $p = 0$, at a time $s = r > 0$, and location $q = -h < 0$. In [50], McKean derived an explicit expression for \mathcal{F} in the case of zero drift by computing the inverse Kontorovich-Lebedev transform of the corresponding renewal equation. In [49], Atkinson and Clifford extended this result to the case of non-zero drift by applying the Radon-Nikodym derivative. Specifically

$$\mathcal{F}(r, h; \varrho) = \frac{\sqrt{3}h}{\pi \varrho r^2} \exp\left(\frac{-1}{2\varrho r} [(r-2)^2 - 2(r-2)(h-1) + 4(h-1)^2]\right) \operatorname{erf}\left(\frac{\sqrt{6h}}{\sqrt{\varrho r}}\right), \quad (4.17)$$

where $\operatorname{erf}(\cdot)$ is the error function. The constant $\varrho > 0$ governs the shape of \mathcal{F} . The limit $\varrho \rightarrow 0$ corresponds to the deterministic case, for which $r = 2$ and $h = 1$. With a small value of ϱ , \mathcal{F} is roughly Gaussian. In contrast, the limit $\varrho \rightarrow \infty$ corresponds to the case of no drift, as in [50], or to the limit $v_2 \rightarrow 0$. In this limit the marginal probability density function for r is asymptotically proportional to $r^{-\frac{5}{4}}$, for large r , and so is long-tailed [49].

In view of the scaling (4.14), the stochastic version of (2.5) corresponding to (4.12) is given by

$$\begin{bmatrix} v_3 \\ w_3 \end{bmatrix} = \begin{bmatrix} -h_i v_2 + \mathcal{O}(2) \\ w_2 + \frac{\gamma_R r_i}{\beta_R} v_2 + \mathcal{O}(2) \end{bmatrix}, \quad (4.18)$$

where r_i and h_i have the joint probability density function (4.17). By combining (4.18) with (2.4) and (2.6) we obtain

$$\begin{bmatrix} u_4 \\ w_4 \end{bmatrix} = \begin{bmatrix} h_i^2 u_1 + \mathcal{O}(3) \\ w_1 - c \left(\frac{\frac{\gamma_L(h_i+1)}{2\beta_L} - \frac{\gamma_R r_i}{2\beta_R}}{\frac{\gamma_L}{\beta_L} - \frac{\gamma_R}{\beta_R}} \right) \sqrt{u_1} + \mathcal{O}(2) \end{bmatrix}, \quad (4.19)$$

which represents the stochastic version of the discontinuity map for points with $u_1 > 0$. Then using (4.19) we arrive at the following stochastic Nordmark map

$$\begin{bmatrix} x_{i+1} \\ y_{i+1} \end{bmatrix} = N_3(x_i, y_i) = \begin{cases} \begin{bmatrix} \tau & 1 \\ -\delta & 0 \end{bmatrix} \begin{bmatrix} x_i \\ y_i \end{bmatrix} + \begin{bmatrix} 0 \\ 1 \end{bmatrix} \mu, & x_i \leq 0 \\ \begin{bmatrix} \tau + a_{11}(h_i^2 - 1) & 1 \\ -\delta h_i^2 & 0 \end{bmatrix} \begin{bmatrix} x_i \\ y_i - \chi \left(\frac{\frac{\gamma_L(h_i+1)}{2\beta_L} - \frac{\gamma_R r_i}{2\beta_R}}{\frac{\gamma_L}{\beta_L} - \frac{\gamma_R}{\beta_R}} \right) \sqrt{x_i} \end{bmatrix} + \begin{bmatrix} 0 \\ 1 \end{bmatrix} \mu, & x_i \geq 0 \end{cases}. \quad (4.20)$$

In (4.20) we treat each pair (r_i, h_i) as a two-dimensional stochastic random variable with probability density function $\mathcal{F}(r_i, h_i; \varrho_i)$, where

$$\varrho_i = \frac{\varepsilon^2 \sqrt{\alpha_L}}{\beta_R \sqrt{2\beta_L} |a_{12}c| \sqrt{x}}, \quad (4.21)$$

which results from combining (4.16) with $v_2 \approx \frac{\sqrt{2\beta_L}}{\sqrt{\alpha_L}} \sqrt{u_1}$, (2.4), and $u_1 = a_{12}^2 c^2 x$, (2.12).

We now estimate the size of the stochastic contribution in N_3 . The leading order stochastic component of N_3 is $\chi \kappa_3(r_i, h_i) \sqrt{x_i}$, where $\kappa_3(r_i, h_i) = \frac{\frac{\gamma_L(h_i+1)}{2\beta_L} - \frac{\gamma_R r_i}{2\beta_R}}{\frac{\gamma_L}{\beta_L} - \frac{\gamma_R}{\beta_R}}$. With (3.6) and $k_{\text{supp}} d = 1$, we can write $\kappa_3(r_i, h_i) \sqrt{x_i} = \sqrt{x_i} + (h_i - 1 - \frac{r_i-2}{2}) \sqrt{x_i}$, where the second term represents the multiplicative stochastic contribution, ignoring the sign of χ , because the deterministic values of h_i and r_i are 1 and 2 respectively.

With a small value of ϱ ($\varrho < 0.03$ is suitable), $\mathcal{F}(r, h; \varrho)$ is approximately Gaussian because the effective noise amplitude in (4.15) is small. By (4.21), this approximation is valid when, roughly speaking, ε is not too large and x_i is not too small. From (4.17) we determine the covariance matrix of the Gaussian approximation to be

$$\text{Cov}(r, h; \varrho) = \frac{2\varrho}{3} \begin{bmatrix} 4 & 1 \\ 1 & 1 \end{bmatrix}, \quad (4.22)$$

and it follows that in this approximation the linear combination $h - \frac{r}{2}$ has standard deviation $\sqrt{\frac{2\varrho}{3}}$. The standard deviation of the stochastic contribution in N_3 is therefore approximately $\sqrt{\frac{2\varrho_i}{3}} \sqrt{x_i}$. Following the previous cases, we write $\varepsilon = \tilde{\varepsilon}_3 \alpha$, and choose $\tilde{\varepsilon}_3$ so that the standard deviation of the stochastic contribution is 0.01 when $\alpha = 1$. For N_3 , this quantity is $\sqrt{\frac{2\varrho_i}{3}} \sqrt{x_i} = x_i^{\frac{1}{4}} \varepsilon \approx 0.46\varepsilon$, using (4.21), the parameter values from Fig. 2, and $x_i = 0.025$. Therefore we let

$$\tilde{\varepsilon}_3 = 0.022. \quad (4.23)$$

Here $\varrho_i \approx 0.008$ when $\alpha = 1$, and so for these values the Gaussian approximation to (4.17) is justified.

Fig. 7 compares iterates of N_3 to intersections with Π' of a numerical solution to (4.8) using $\varepsilon = \tilde{\varepsilon}_3$. As with the previous two figures, this shows that N_3 can accurately capture the stochastic dynamics of (4.8).

5 Stochastic dynamics

In this section we explore the dynamics of the three stochastic Nordmark maps, N_1 , N_2 and N_3 , and discuss how the different forms of these maps is evident in their dynamical behaviour. To briefly summarise, N_1 applies to the system with stochastic switching (4.3), whereas N_2 and N_3 apply to (4.8). For N_1 and N_2 it is assumed that the value of ν (the correlation time of the noise) is large relative to the times that orbits spend in $u > 0$. As these times are rarely larger than $t = 0.05$ for the parameter values considered here, we take $\nu = 0.5$ in N_1 and N_2 to ensure that the correlation time is large enough. The values of ξ_i in N_1 and N_2 are distributed according to

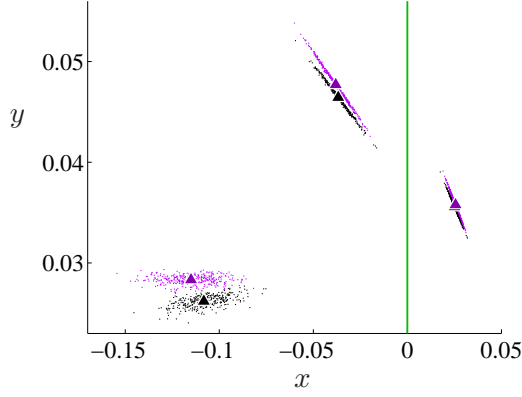


Figure 7: A phase portrait comparing the stochastic return map N_3 with a numerical solution to (4.8). The three groups of purple dots were obtained by numerically solving (4.8) with (4.1), $\nu = 0$ (in which case $\xi(t) dt$ is replaced by $\varepsilon dW(t)$) and $\varepsilon = \tilde{\varepsilon}_3$, for the vibro-impacting system (3.1) with (3.5) using the same parameter values as in Fig. 5. The three groups of black dots are 1000 iterates of N_3 with (4.17) and (4.21) and parameter values matching those of the vibro-impacting system. The deterministic 3-cycles of (4.3) and (4.6) are shown with triangles.

(4.4). N_3 corresponds to the limit $\nu \rightarrow 0$. In N_3 , r_i and h_i are distributed according to (4.17) and depend on the value of ρ_i (4.21).

For each N_j we have written

$$\varepsilon = \tilde{\varepsilon}_j \alpha, \quad (5.1)$$

where the $\tilde{\varepsilon}_j$ are given by (4.7), (4.11) and (4.23). These values have been chosen such that for a given value of α , the size of the stochastic contribution in N_1 , N_2 and N_3 is roughly the same, at least when $\mu = 0.03$. For μ close to 0, the stochastic contributions are noticeably different for these choices of $\tilde{\varepsilon}_j$.

In §5.1 we look at stochastic bifurcation diagrams in order to obtain a basic understanding of how the stochastic dynamics differs with the value of μ . In the subsequent parts of this section we study two-dimensional invariant densities in order to gain a deeper understanding of the dynamics.

5.1 The dependence of μ on the size of noise response

Fig. 8 shows stochastic versions of the bifurcation diagram shown in Fig. 2 for the three stochastic Nordmark maps. As expected, the noise blurs the bifurcation diagram. In panel A, which corresponds to the map N_1 , for values of μ very close to zero (say $|\mu| < 0.002$) the points are relatively highly spread. This is because here the deterministic map has an attractor near $x = 0$, so in N_1 the sign of x_i is often different to the sign of $x_i + \frac{\xi_i}{a_{12}^2 c^2}$. That is, the choice of the half-map of N_1 is regularly determined by ξ_i rather than x_i . Furthermore, as shown in §4.1, the leading order component of the stochastic contribution to the right half-map of N_1 is inversely proportional to $\sqrt{x_i}$, which for very small μ is large relative to its value for μ away from zero. In contrast, with $0.03 \leq \mu \leq 0.05$ say, the underlying attracting 3-cycle is sufficiently far from $x = 0$ so that the sign of x_i rarely differs from that of $x_i + \frac{\xi_i}{a_{12}^2 c^2}$. The points are randomly distributed

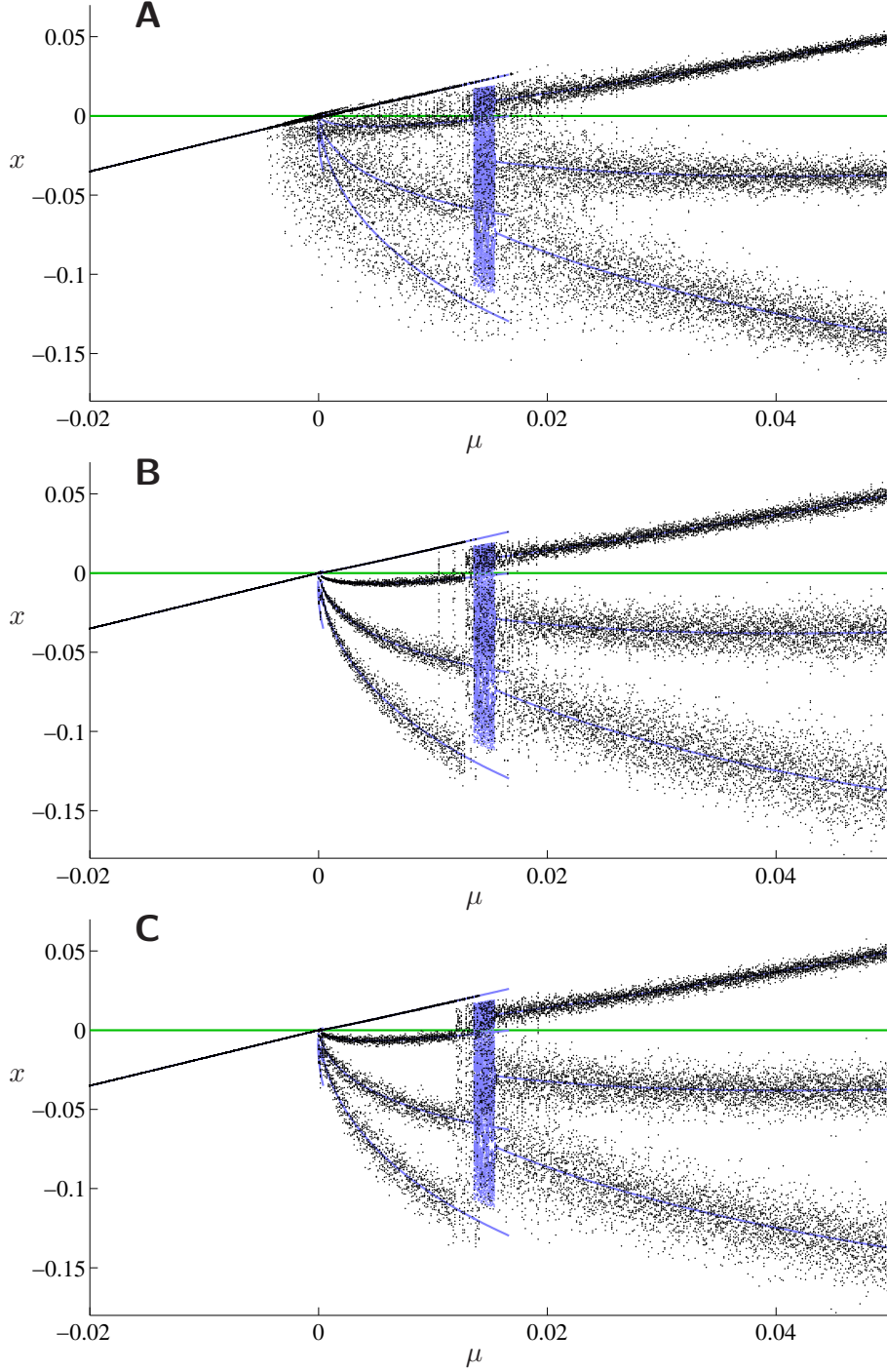


Figure 8: Bifurcation diagrams of the stochastic Nordmark maps N_1 (panel A), N_2 (panel B), and N_3 (panel C), with $\tau \approx 0.5813$, $\delta \approx 0.1518$, and $\chi = 1$. These parameter values correspond to the vibro-impacting system (3.1), with $(k_{\text{osc}}, b_{\text{osc}}, k_{\text{supp}}, b_{\text{supp}}, d) = (4.5, 0.3, 10, 0, 0.1)$. The black dots are iterates of N_1 , N_2 and N_3 with transient points omitted. The noise amplitudes are given by (4.7), (4.11) and (4.23) with $\alpha = 1$, and $\nu = 0.5$ for panels A and B (panel C corresponds to $\nu = 0$). In each panel the deterministic bifurcation diagram (Fig. 2) is shown in blue.

about the 3-cycle due to noise in the right half-map of N_1 . The size of the deviation decreases with increasing μ , because the strength of attraction of the 3-cycle increases with μ .

In panels B and C, which correspond to N_2 and N_3 respectively, the bifurcation diagrams show no variability for $\mu < 0$. This is because for $\mu < 0$, (x^L, y^L) (1.5) is a fixed point of N_2 and N_3 . For $0.002 \leq \mu \leq 0.01$, the size of deviations about the underlying attracting 4-cycle increases with μ . This is primarily because the coefficient of the \sqrt{x} -term of N_2 and N_3 is random, and for the 4-cycle this value of x increases with μ . For $0.03 \leq \mu \leq 0.05$, the size of deviations varies little with μ because the increased variability caused by a larger value of x is balanced by the fact that the strength of attraction of the 3-cycle increases. Panels B and C are similar, suggesting that the value of ν has little effect on the long-term dynamics, although panel C shows slightly more variability for very small values of $\mu > 0$.

5.2 Invariant densities about an attracting periodic solution

Figs. 9-14 show two-dimensional invariant densities of N_1 , N_2 and N_3 . By assuming ergodicity, invariant densities were computed on a 256×256 grid of x and y values from 10^8 consecutive

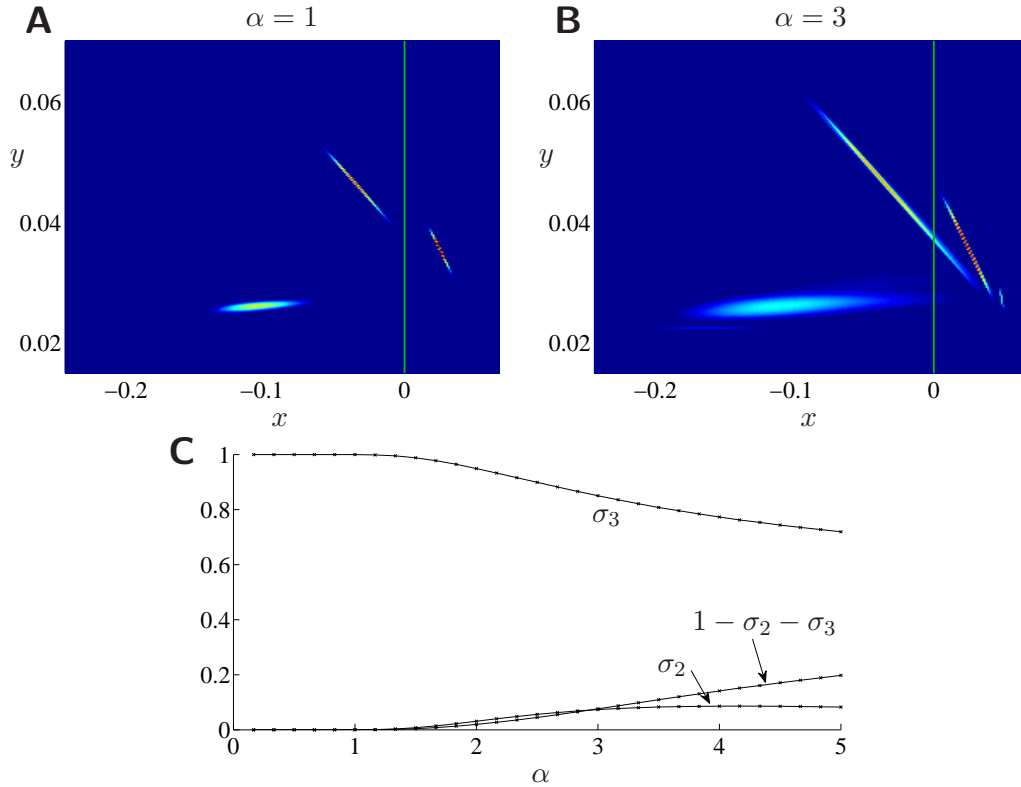


Figure 9: Panel A shows the invariant density of N_1 with the same parameter values as Fig. 8 and $\mu = 0.03$. The value of the density is indicated by colour (dark red – the maximum value of the density; dark blue – zero). Panel B shows the invariant density at three times the noise amplitude as panel A. Panel C plots σ_j – the fraction of instances that points return to $x > 0$ in j iterations (5.2) – against the noise amplitude.

iterates of a single orbit with transient points omitted.

Let us first explain panel C of Figs. 9-11. Given a sample orbit of N_1 , N_2 or N_3 , for each point with $x_i > 0$ we let \mathcal{I}_i be the smallest positive integer for which $x_{i+\mathcal{I}_i} > 0$, as in [37]. \mathcal{I}_i represents the number of iterations required for a return to $x > 0$ from the point (x_i, y_i) . Numerically we can compute a large number of values of \mathcal{I}_i (say M of them). Then for each $j \in \mathbb{Z}^+$, we let σ_j denote the fraction of the \mathcal{I}_i that are equal to j , i.e.

$$\sigma_j = \frac{1}{M} \sum_{i \text{ with } x_i > 0} \chi_{j-\mathcal{I}_i}, \quad (5.2)$$

where $\chi_k = 1$ if $k = 0$, and $\chi_k = 0$ otherwise. Figs. 9-11 correspond to $\mu = 0.03$ for which there is an underlying attracting 3-cycle. Therefore with small noise, $\sigma_3 \approx 1$, and for all $j \neq 3$, $\sigma_j \approx 0$.

Fig. 9 corresponds to the map N_1 . In panel A, the size of the noise is relatively small, so iterates of N_1 follow close to the 3-cycle. The invariant density is well-approximated by a scaled sum of three Gaussian densities centred at each point of the 3-cycle. About the point with $x \approx -0.1$, the density is stretched substantially more in x -direction than in the y -direction. This is because points with $x \approx -0.1$ have likely just undergone an iteration under the right half-map of N_1 which is stochastic in the x -component but not the y -component. The stretching around other iterates is then a consequence of iterating under N_1 with $x < 0$.

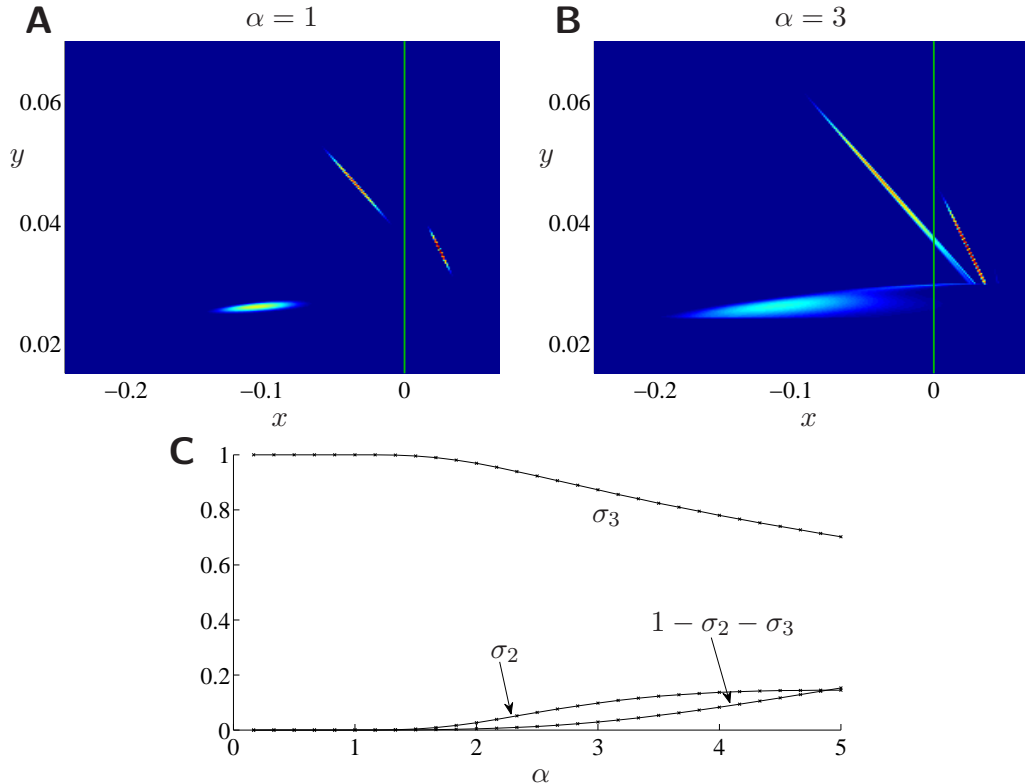


Figure 10: Panel A shows the invariant density of N_2 with the same parameter values as Fig. 8 and $\mu = 0.03$. Panel B shows the invariant density with $\alpha = 3$, and panel C is a plot of the fractions σ_j (5.2).

With larger values of α , it is relatively common for the orbit to return to $x > 0$ in a number of iterations other than three, Fig. 9-C. For this reason the invariant density displays additional characteristics. For instance with $\alpha = 3$, the orbit returns to $x > 0$ in two iterations almost 10% of the time. Consequently, a substantial part of the invariant density centred roughly about the point of the 3-cycle with $x \approx -0.04$, lies in $x > 0$, Fig. 9-B. The invariant density in panel B also has a small component with $x \approx 0.05$. This is due to points of the orbit with small values of $x > 0$ mapping under the left half-map of N_1 due to the noise (i.e. returning to $x > 0$ in only one iteration).

Fig. 10 illustrates N_2 using the same parameter values. Again with small noise the invariant density is roughly Gaussian about each point of the 3-cycle, whereas for relatively large noise iterates often cross into $x > 0$ prematurely causing the invariant density to take an irregular shape. When $\alpha = 3$, points of the orbit that do not return to $x > 0$ in three iterations, usually return to $x > 0$ in two iterations.

Fig. 11 corresponds to N_3 and is similar to the previous figure. This indicates that the correlation time ν has little effect on these pictures, although the invariant density has a slightly different shape when $\alpha = 3$.

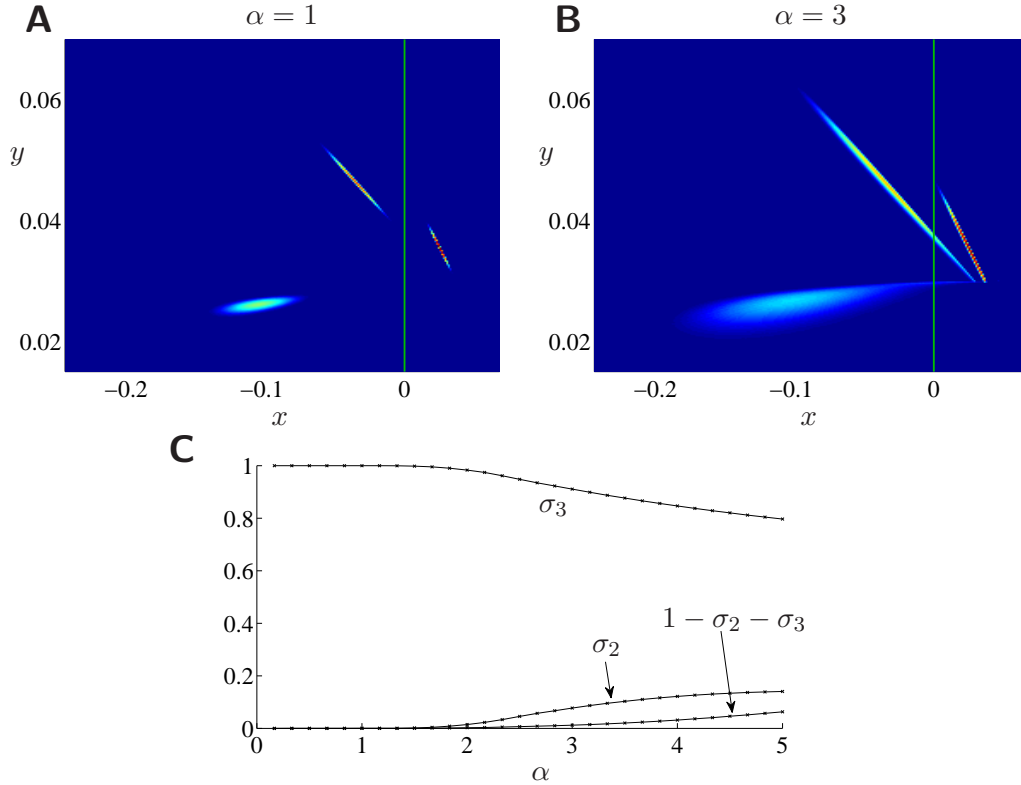


Figure 11: Panel A shows the invariant density of N_3 with the same parameter values as Fig. 8 and $\mu = 0.03$. Panel B shows the invariant density with $\alpha = 3$, and panel C is a plot of the fractions σ_j (5.2).

5.3 Invariant densities near the grazing bifurcation

Fig. 12 shows invariant densities of N_1 , N_2 and N_3 for parameter values closer to the grazing bifurcation than the previous three figures, specifically $\mu = 0.001$. At this value of μ , there is an underlying attracting 4-cycle, panel A. The noise amplitudes are given by (4.7), (4.11) and (4.23) with $\alpha = 1$. Recall, these amplitudes were chosen such that the size of the noise response of the three maps is roughly the same for larger values of μ . Here, however, the size of noise response differs substantially. In panels C and D, which correspond to N_2 and N_3 respectively, the invariant density is approximately a scaled sum of four Gaussians about each point of the 4-cycle. The invariant density in panel D, corresponding to $\nu = 0$, is noticeably larger than that of panel C.

In panel B, which corresponds to N_1 , the noise has a substantial effect because the switching condition of N_1 is stochastic, and many points of N_1 fall close to $x = 0$. The invariant density has a small C-shaped component in $x > 0$ corresponding to consecutive points of the orbit mapping under the left half-map of N_1 . The part of the invariant density for $x < 0$ and $y \approx 0.001$ corresponds to images of points under the right half-map of N_1 , and is bimodal because the invariant density has roughly two components in $x > 0$.

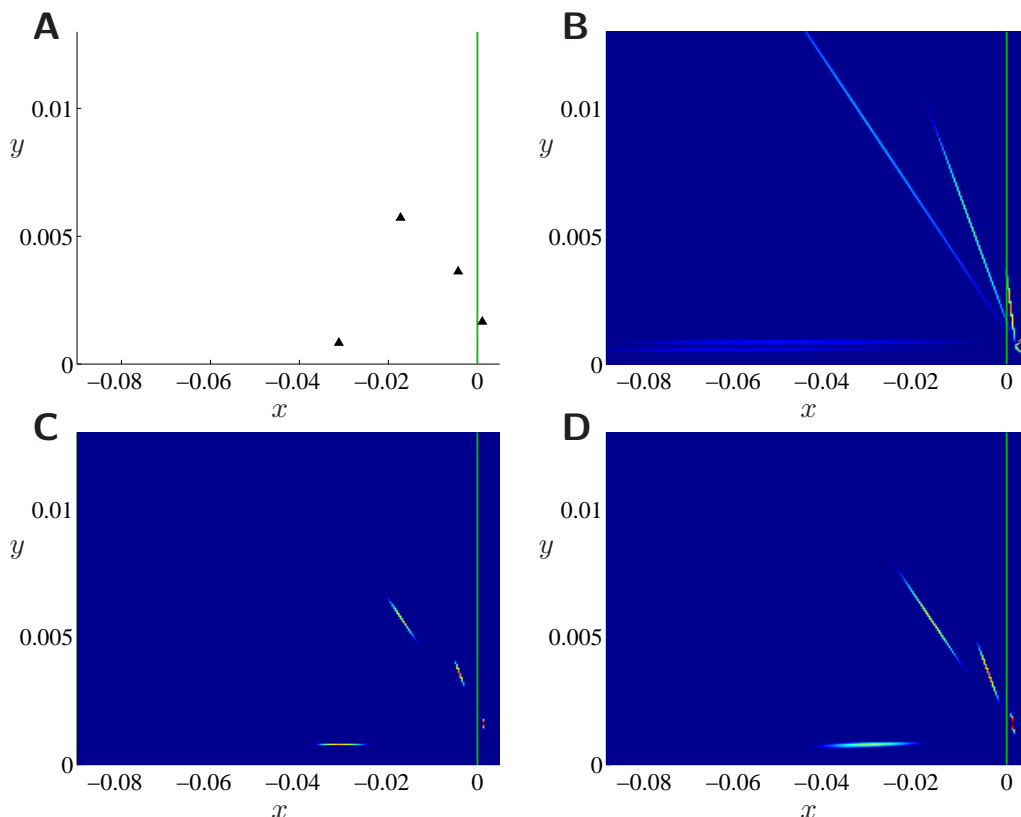


Figure 12: Panel A shows the attracting 4-cycle of (1.3) with the same parameter values as Fig. 2 and $\mu = 0.001$. Panels B, C and D show the invariant densities of N_1 , N_2 and N_3 , respectively, using the same parameter values as Fig. 8 and $\mu = 0.001$.

5.4 Invariant densities about coexisting attractors

With $\mu = 0.0145$ in Fig. 2, there is an attracting 4-cycle and an apparently chaotic attractor. These are shown in Fig. 13-A. As with smooth maps [51, 52], in the presence of noise orbits commonly dwell near the attractors for relatively long periods of time, and switch between attractors quickly. Invariant densities of N_1 , N_2 and N_3 are shown in panels B, C and D. In each case the bulk of the density is centred about the two underlying attractors. With white noise (panel D) there is no gap in the invariant density around $(x, y) \approx (-0.12, 0.012)$ due to randomness in both the x and y -components of N_3 .

Lastly, Fig. 14 illustrates stochastic dynamics with $\mu < 0$. This figure corresponds to $k_{\text{osc}} = 5$ (different to Fig. 2) and $\mu = -0.002$ at which N has an attracting 3-cycle as well as the attracting fixed point (x^L, y^L) (1.5). These are shown in panel A. The dynamics of N_2 and N_3 for $x < 0$ is deterministic, hence (x^L, y^L) is a fixed point of these maps. Given an initial point (x_0, y_0) near the 3-cycle, sample orbits of N_2 and N_3 eventually reach (x^L, y^L) . In contrast, N_1 has an invariant density concentrated about the two attractors, panel B. The part of the density with $x \approx 0$ and $y < y_L$ corresponds to points of the orbit repeatedly following the left half-map of N_1 (with $x_i < 0$ and $x_i + \frac{\xi_i}{a_{12}^2 c^2} < 0$).

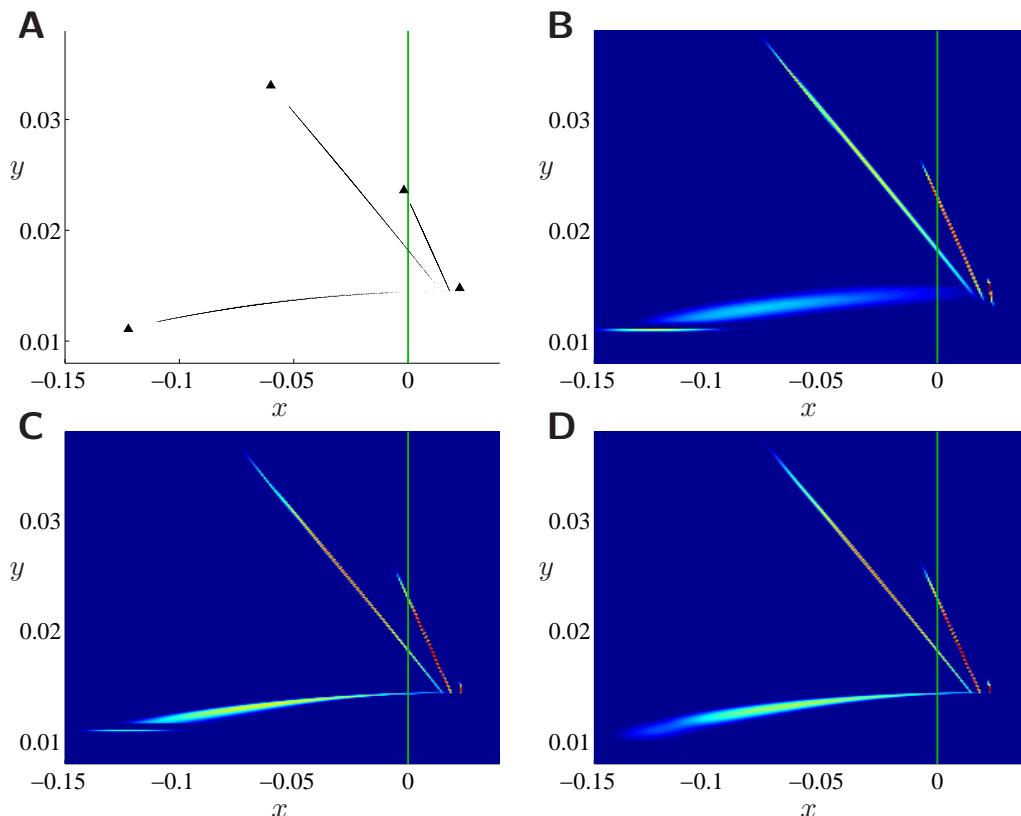


Figure 13: Panel A shows an attracting 4-cycle and a numerically computed attractor of (1.3) with the same parameter values as Fig. 2 and $\mu = 0.0145$. Panels B, C and D show the invariant densities of N_1 , N_2 and N_3 , respectively, with the same parameter values as Fig. 8 and $\mu = 0.0145$.

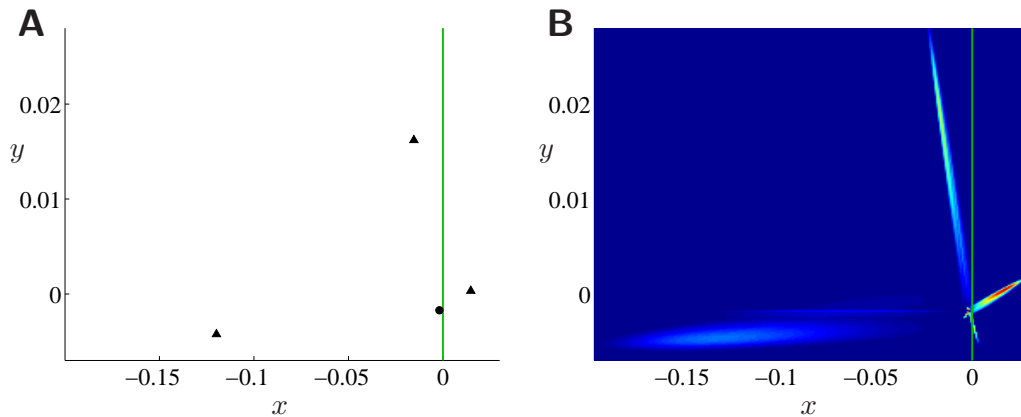


Figure 14: Panel A shows the attracting fixed point (x^L, y^L) (1.5) and the attracting 3-cycle of N with the same parameter values as Fig. 2, except $k_{\text{osc}} = 5$ and $\mu = -0.002$. Here $\tau \approx 0.0927$, $\delta \approx 0.1518$ and $\chi = 1$. Panel B shows the invariant density of the corresponding map N_1 , with $\nu = 0.5$ and $\varepsilon = 0.0005$.

6 Conclusions

This paper concerns grazing bifurcations for which the associated dynamics is described by the Nordmark map (1.3). The potential influence of randomness and uncertainties on the dynamics of (1.3) was described in [37] by studying (1.3) in the presence of additive white Gaussian noise. Such a noise formulation is suitable if the nature of the randomness in the ODE system is practically independent to the state of the system, such as if there is a random forcing term.

In this paper we considered the alternate scenario that randomness is present in the switching condition of the ODE system, and in f_R – the part of the vector field opposite to the tangential intersection of the grazing periodic orbit. These cases are especially relevant for vibro-impacting systems for which impact events represent the primary source of uncertainty. We derived three different stochastic versions of (1.3). These are the maps N_1 (4.6), which corresponds to a noisy switching condition in the ODE system, N_2 (4.10), which corresponds to noise in f_R with a large correlation time, and N_3 (4.20), which corresponds to white noise in f_R . In each case the noise is nonlinear and non-additive. This indicates that some diligence should be taken when formulating stochastic return maps for grazing bifurcations of piecewise-smooth systems.

The stochastic dynamics of N_1 , N_2 and N_3 differs in many ways to that of (1.3) with additive noise, described in [37]. For N_1 , N_2 and N_3 , dynamics prior to the grazing bifurcation is deterministic, and beyond the grazing bifurcation two-dimensional invariant densities are often skewed dramatically so that they appear almost one-dimensional.

Near the grazing bifurcation, N_1 exhibits a large noise response relative to N_2 and N_3 . This suggests that if experimental data of a physical system shows relatively high variability near a grazing bifurcation, then it is likely to be most appropriate to include randomness in the switching condition of a mathematical model. Invariant densities of N_1 near grazing are highly irregular due to the randomness in the switching condition. For N_2 and N_3 , the size of the noise response increases, for most part, with the distance (in parameter space) beyond the grazing bifurcation. The maps N_2 and N_3 exhibit qualitatively similar invariant densities, which implies that the correlation time has little effect. Indeed the correlation time only influences the short-

time dynamics of (4.8) with $u > 0$, and the precise nature of these dynamics has a negligible effect on the invariant densities, which relate to long-time dynamics.

References

- [1] J. Awrejcewicz and C. Lamarque. *Bifurcation and Chaos in Nonsmooth Mechanical Systems*. World Scientific, Singapore, 2003.
- [2] B. Blazejczyk-Okolewska, K. Czołczynski, T. Kapitaniak, and J. Wojewoda. *Chaotic Mechanics in Systems with Impacts and Friction*. World Scientific, Singapore, 1999.
- [3] B. Brogliato. *Nonsmooth Mechanics: Models, Dynamics and Control*. Springer-Verlag, New York, 1999.
- [4] R.A. Ibrahim. *Vibro-Impact Dynamics*, volume 43 of *Lecture Notes in Applied and Computational Mechanics*. Springer, New York, 2009.
- [5] M. Wiercigroch and B. De Kraker, editors. *Applied Nonlinear Dynamics and Chaos of Mechanical Systems with Discontinuities*, Singapore, 2000. World Scientific.
- [6] M.P. Païdoussis and G.X. Li. Cross-flow-induced chaotic vibrations of heat-exchanger tubes impacting on loose supports. *J. Sound Vib.*, 152(2):305–326, 1992.
- [7] J.M. de Bedout, M.A. Franchek, and A.K. Bajaj. Robust control of chaotic vibrations for impacting heat exchanger tubes in crossflow. *J. Sound Vib.*, 227(1):183–204, 1999.
- [8] I. Grabec. Chaotic dynamics of the cutting process. *Int. J. Mach. Tools Manufact.*, 28(1):19–32, 1988.
- [9] M. Wiercigroch. Chaotic vibration of a simple model of the machine tool-cutting process system. *J. Vib. Acoust.*, 119(3):468–475, 1997.
- [10] B. Balachandran. Nonlinear dynamics of milling processes. *Phil. Trans. R. Soc. Lond. A*, 359:793–819, 2001.
- [11] H. Dankowicz, X. Zhao, and S. Misra. Near-grazing dynamics in tapping-mode atomic-force microscopy. *Int. J. Non-Linear Mech.*, 42(4):697–709, 2007.
- [12] A. Raman, J. Melcher, and R. Tung. Cantilever dynamics in atomic force microscopy. *Nanotoday*, 3(1-2):20–27, 2008.
- [13] S. Misra, H. Dankowicz, and M.R. Paul. Degenerate discontinuity-induced bifurcations in tapping-mode. *Phys. D*, 239:33–43, 2010.
- [14] D.E. Stewart. Rigid-body dynamics with friction and impact. *SIAM Rev.*, 42(1):3–39, 2000.
- [15] W.J. Stronge. *Impact Mechanics*. Cambridge University Press, New York, 2004.

- [16] R. Alzate, M. di Bernardo, U. Montanaro, and S. Santini. Experimental and numerical verification of bifurcations and chaos in cam-follower impacting systems. *Nonlinear Dyn.*, 50(3):409–429, 2007.
- [17] R. Alzate, M. di Bernardo, G. Giordano, G. Rea, and S. Santini. Experimental and numerical investigation of coexistence, novel bifurcations, and chaos in a cam-follower system. *SIAM J. Appl. Dyn. Sys.*, 8(2):592–623, 2009.
- [18] P.T. Piiroinen, L.N. Virgin, and A.R. Champneys. Chaos and period-adding: Experimental and numerical verification of the grazing bifurcation. *J. Nonlin. Sci.*, 14(4):383–404, 2004.
- [19] J. Ing, E. Pavlovskaja, and M. Wiercigroch. Dynamics of a nearly symmetrical piecewise linear oscillator close to grazing incidence: Modelling and experimental verification. *Nonlinear Dyn.*, 46:225–238, 2006.
- [20] J. Ing, E. Pavlovskaja, M. Wiercigroch, and S. Banerjee. Experimental study of impact oscillator with one-sided elastic constraint. *Phil. Trans. R. Soc. A*, 366:679–704, 2008.
- [21] J. Ing, E. Pavlovskaja, M. Wiercigroch, and S. Banerjee. Bifurcation analysis of an impact oscillator with a one-sided elastic constraint near grazing. *Phys. D*, 239:312–321, 2010.
- [22] A.J. Van der Schaft and J.M. Schumacher. *An Introduction to Hybrid Dynamical Systems*. Springer-Verlag, New York, 2000.
- [23] M. di Bernardo, C.J. Budd, A.R. Champneys, and P. Kowalczyk. *Piecewise-smooth Dynamical Systems. Theory and Applications*. Springer-Verlag, New York, 2008.
- [24] A.B. Nordmark. Non-periodic motion caused by grazing incidence in impact oscillators. *J. Sound Vib.*, 2:279–297, 1991.
- [25] A.B. Nordmark. Universal limit mapping in grazing bifurcations. *Phys. Rev. E*, 55(1):266–270, 1997.
- [26] A.B. Nordmark. Existence of periodic orbits in grazing bifurcations of impacting mechanical oscillators. *Nonlinearity*, 14:1517–1542, 2001.
- [27] R.I. Leine and D.H. Van Campen. Discontinuous bifurcations of periodic solutions. *Math. Comput. Model.*, 36:259–273, 2002.
- [28] C.J. Budd and P.T. Piiroinen. Corner bifurcations in non-smoothly forced impact oscillators. *Phys. D*, 220:127–145, 2006.
- [29] M. Oestreich, N. Hinrichs, K. Popp, and C.J. Budd. Analytical and experimental investigation of an impact oscillator. In *Proceedings of the ASME 16th Biennial Conf. on Mech. Vibrations and Noise.*, pages 1–11, 1997.
- [30] M.F. Dimentberg and A.I. Menyailov. Response of a single-mass vibroimpact system to white-noise random excitation. *Z. Angew. Math. Mech.*, 59(12):709–716, 1979.

- [31] J.B. Roberts and P.D. Spanos. Stochastic averaging: An approximate method of solving random vibration problems. *Int. J. Non-Linear Mechanics*, 21(2):111–134, 1986.
- [32] M. Fogli, P. Bressollette, and P. Bernard. The dynamics of a stochastic oscillator with impacts. *Eur. J. Mech. A-Solids*, 15(2):213–241, 1996.
- [33] M.F. Dimentberg and D.V. Iourtchenko. Random vibrations with impacts: A review. *Non-linear Dyn.*, 36:229–254, 2004.
- [34] T.C.L. Griffin. *Dynamics of Stochastic Nonsmooth Systems*. PhD thesis, University of Bristol, 2005.
- [35] G. Mayer-Kress and H. Haken. The influence of noise on the logistic model. *J. Stat. Phys.*, 26(1):149–171, 1981.
- [36] J.P. Crutchfield, J.D. Farmer, and B.A. Huberman. Fluctuations and simple chaotic dynamics. *Phys. Rep.*, 92(2):45–82, 1982.
- [37] D.J.W. Simpson, J. Hogan, and R. Kuske. Stochastic regular grazing bifurcations. *SIAM J. Appl. Dyn. Sys.*, 12(2):533–559, 2013.
- [38] M. di Bernardo, C.J. Budd, and A.R. Champneys. Normal form maps for grazing bifurcations in n -dimensional piecewise-smooth dynamical systems. *Phys. D*, 160:222–254, 2001.
- [39] J. Molenaar, J.G. de Weger, and W. van de Water. Mappings of grazing-impact oscillators. *Nonlinearity*, 14:301–321, 2001.
- [40] Y. Ma, M. Agarwal, and S. Banerjee. Border collision bifurcations in a soft impact system. *Phys. Lett. A*, 354:281–287, 2006.
- [41] Y. Ma, J. Ing, S. Banerjee, M. Wiercigroch, and E. Pavlovskaya. The nature of the normal form map for soft impacting systems. *Int. J. Nonlinear Mech.*, 43:504–513, 2008.
- [42] P. Hänggi and P. Jung. Colored noise in dynamical systems. In I. Prigogine and S.A. Rice, editors, *Advances in Chemical Physics.*, volume 89, pages 239–326. John Wiley & Sons, New York, 1995.
- [43] E.-K. Boukas. *Stochastic Switching Systems. Analysis and Design*. Birkhäuser, Boston, 2006.
- [44] D. Liberzon. *Switching in Systems and Control*. Birkhäuser, Boston, 2003.
- [45] P. Glendinning. The border collision normal form with stochastic switching surface. *SIAM J. Appl. Dyn. Sys.*, 13(1):181–193, 2014.
- [46] J. Grasman and O.A. van Herwaarden. *Asymptotic Methods for the Fokker-Planck Equation and the Exit Problem in Applications*. Springer, New York, 1999.
- [47] S. Redner. *A Guide to First-Passage Processes*. Cambridge University Press, New York, 2001.

- [48] Z. Schuss. *Theory and Applications of Stochastic Processes*. Springer, New York, 2010.
- [49] R.A. Atkinson and P. Clifford. The escape probability for integrated Brownian motion with non-zero drift. *J. Appl. Prob.*, 31:921–929, 1994.
- [50] Jr. H.P. McKean. A winding problem for a resonator driven by a white noise. *J. Math. Kyoto Univ.*, 2(2):227–235, 1963.
- [51] E. Knobloch and J.B. Weiss. Effect of noise on discrete dynamical systems with multiple attractors. In M.F. McClintock and P.V.E. Moss, editors, *Noise in Nonlinear Dynamical Systems. Theory of noise induced processes in special applications.*, volume 2, pages 65–86. Cambridge University Press, New York, 1989.
- [52] S. Kraut, U. Feudel, and C. Grebogi. Preference of attractors in noisy multistable systems. *Phys. Rev. E*, 59(5):5253–5260, 1999.